ENGINEERING

Skin-attached haptic patch for versatile and augmented tactile interaction

Jung-Hwan Youn[1,2,3], Seung-Yeon Jang[1,2], Inwook Hwang[2], Qibing Pei[4], Sungryul Yun[2]*, Ki-Uk Kyung[1]*

Wearable tactile interfaces can enhance immersive experiences in virtual/augmented reality systems by adding tactile stimulation to the skin along with the visual and auditory information delivered to the user. We introduce a flat cone dielectric elastomer actuator (FCDEA) array that is thin, soft, and capable of producing spatiotemporally adjustable and large static-to-dynamic force in response to electric voltage signals on large areas of the skin. Integration of the FCDEA array into a photomicrosensor array enables the implementation of a wearable wireless communication haptic patch. We demonstrate that the developed haptic patch allows users to communicate tactile information in real time while maintaining conformal contact with the skin. The haptic patch can also express the topology of 3D structures and render textures of virtual objects in response to localized vibration of the FCDEA array. We expect that the developed haptic patch will provide an immersive touching experience in virtual reality and facilitate tactile communication between users in various applications.

INTRODUCTION

Virtual reality (VR) and augmented reality (AR) technologies that enable users to interact in virtual worlds have become easily accessible in daily life for various purposes, such as entertainment, education, medicine, training, and rehabilitation (*1*, *2*). However, VR/AR scenarios that only allow audiovisual feedback without physical interactions present limitations in providing realistic experiences. Tactile feedback linked to audiovisual information is an indispensable modality toward more immersive interactions of users with virtual environments (*3*).

A glove-typed tactile interface using microfluidic actuation called HaptX Gloves G1 (*4*) can provide tactile feedback to more than 100 areas on the hand, but it involves a bulky system that includes an external compressor. Recently, tactile feedback interfaces that provide cutaneous stimuli have been developed into thin flexible structures that can be integrated into the skin while reducing interference with the dynamic motion of the user (*5*, *6*). Various driving forces such as electric (*7*), electromagnetic (*8*–*11*), electrohydraulic (*12*–*15*), piezoelectric (*16*, *17*), pneumatic (*18*, *19*), thermal (*20*), and dielectric elastomer (DE) force (*21*–*29*) have been used to deliver tactile feedback in wearable platforms.

Among tactile stimulation strategies, dielectric elastomer actuators (DEAs) have received great attention owing to their fast deformation response, which enables generating vibrations over a wide frequency range in a soft and lightweight design (*30*–*32*). Multilayered DEAs can generate tactile sensations over a wide frequency band of 0 to 500 Hz, even in an ultrathin lightweight structure (*21*–*23*). A wearable device for the finger and connecting a multilayered DEA to a battery and photodiode showcased the ability to identify the direction and position of letters through tactile exploration (*23*). A single hydraulic coupled DEA integrated into a plastic case delivered the tactile sensation of touching soft bodies to a fingertip in virtual environments (*24*, *25*). Rolled DEAs in a 2 × 2 array were used for wearable haptic communication on the forearm (*26*). Double-cone DEAs with a rigid pillar between the DEA and a passive membrane were used in wearable displays for fingertip tactile interaction (*27*–*29*). Although most existing DEAs have excellent actuation speeds and provide suitable softness for skin-integrated tactile interfaces, they lack the output force required to overcome the damping effect of the skin over a wide frequency band. Consequently, their performance is reduced by both miniaturization of the active areas and formation of a structure conformally adhered to the skin (*33*–*35*). Moreover, the absence of tactile sensing capability makes it difficult for DEA-based wearable tactile interfaces to enable tactile communication between users or between users and avatars in a virtual environment beyond providing tactile feedback (*21*–*29*).

We introduce a thin, lightweight, and soft flat-cone DEA (FCDEA) array that can produce large spatiotemporally patternable wireless tactile feedback over a wide frequency band via programmable out-of-plane deformation of individual active areas in response to electric voltage signals, enabling wireless tactile communication (see movie S1). The proposed FCDEA consists of a multilayered DEA membrane coupled with a compression spring constructed from spiral flexures. This spring converts the area expansion of the multilayered DEA caused by electrostatic pressure into a linear deformation. By exploiting the elastic restoring force of the thin compression spring, the FCDEA produces a high actuation strain (>77%) in an extremely thin form factor (1.1 mm) while exhibiting a higher power density (2.09 kW/kg) than other DEAs. The minimum perception thresholds for force and displacement at the fingertips are approximately 15 mN and 10 μm for quasi-static stimuli and 1.7 mN and 1.7 μm for vibrotactile stimuli in the 250- to 320-Hz range, respectively (*12*, *36*, *37*). To ensure haptic sensations that are easily perceivable across a broad range of users, haptic actuators should exceed these thresholds by at least 10 times (20 dB) (*12*). Compared to these requirements, the FCDEA generates large force (323 mN at 0.1 Hz and 2.2 N at 280 Hz) and displacement (849 μm at 0.1 Hz and 310 μm at 280 Hz). In addition,

[1]Department of Mechanical Engineering, Korea Advanced Institute of Science and Technology, Daejeon, South Korea. [2]Tangible Interface Creative Research Section, Electronics and Telecommunications Research Institute, Daejeon, South Korea. [3]Department of Electrical and Computer Engineering, University of Illinois Urbana-Champaign, IL, USA. [4]Department of Materials Science and Engineering, Henry Samueli School of Engineering and Applied Science, University of California Los Angeles, CA, USA.
*Corresponding author. Email: kyungku@kaist.ac.kr (K.-U.K.); sungryul@etri.re.kr (S.Y.)

the FCDEA has a mechanical impedance similar to that of the human fingertip skin, which is advantageous for optimizing the energy efficiency along with the natural tactile interaction (*38*). We integrate a dense array of FCDEAs on a 6-mm pitch into a flexible printed circuit board (PCB), enabling conformal contact with the skin by virtue of its flexibility and thin form factor. Tactile sensing is achieved by integrating a reflective photomicrosensor array with the FCDEA array. The integrated haptic patch can provide bidirectional wireless tactile communication in a VR environment or between users by encoding tactile information and reproducing tactile sensations on the hands.

RESULTS

Design concept of haptic patch

Existing tactile interfaces cannot faithfully convey a realistic sense of touch due to limitations of the tactile actuators in achieving high spatial resolution, large actuation strain and output power, low power consumption, and a wide operating frequency range (0 to 500 Hz). To meet these demanding requirements in a wearable tactile interface, we introduce an FCDEA comprising a multilayered DEA membrane and compression spring, as illustrated in Fig. 1A. This design merges the advantages of large-area strain of the DEA membrane with the highly elastic nature of a compression spring, allowing to produce a large out-of-plane deformation, as illustrated in Fig. 1B. The compression spring was required to have a thin form factor to maximize the actuation strain of FCDEA (see fig. S1 and Supplementary Text). In parallel, the multilayered stacking of DEA membranes was required to enhance the output force and output power. Figure 1C shows that the proposed FCDEA provides both higher actuation strain and power density (power-to-weight ratio) than other soft actuators (*8*, *13*, *20*, *22*, *26*, *27*, *39*–*41*).

The compact size and thin form factor of the FCDEA render it promising for wearable tactile interfaces, particularly in dense arrays, as illustrated in Fig. 1D. The integration of a photomicrosensor array with the FCDEA enables user to perceive and transmit the tactile information to another user, as illustrated in Fig. 1D. To facilitate intimate and conformal contact with the skin, both the actuator and sensor array are integrated into a flexible PCB, as depicted in Fig. 1E. Once in contact, the FCDEAs can deliver localized pressure and vibrational feedback to the user owing to their ability to generate a large output force over a broad frequency range (0.1 to 500 Hz) (Fig. 1F). As illustrated in Fig. 1G, the proposed FCDEA array can express static and dynamic information, such as

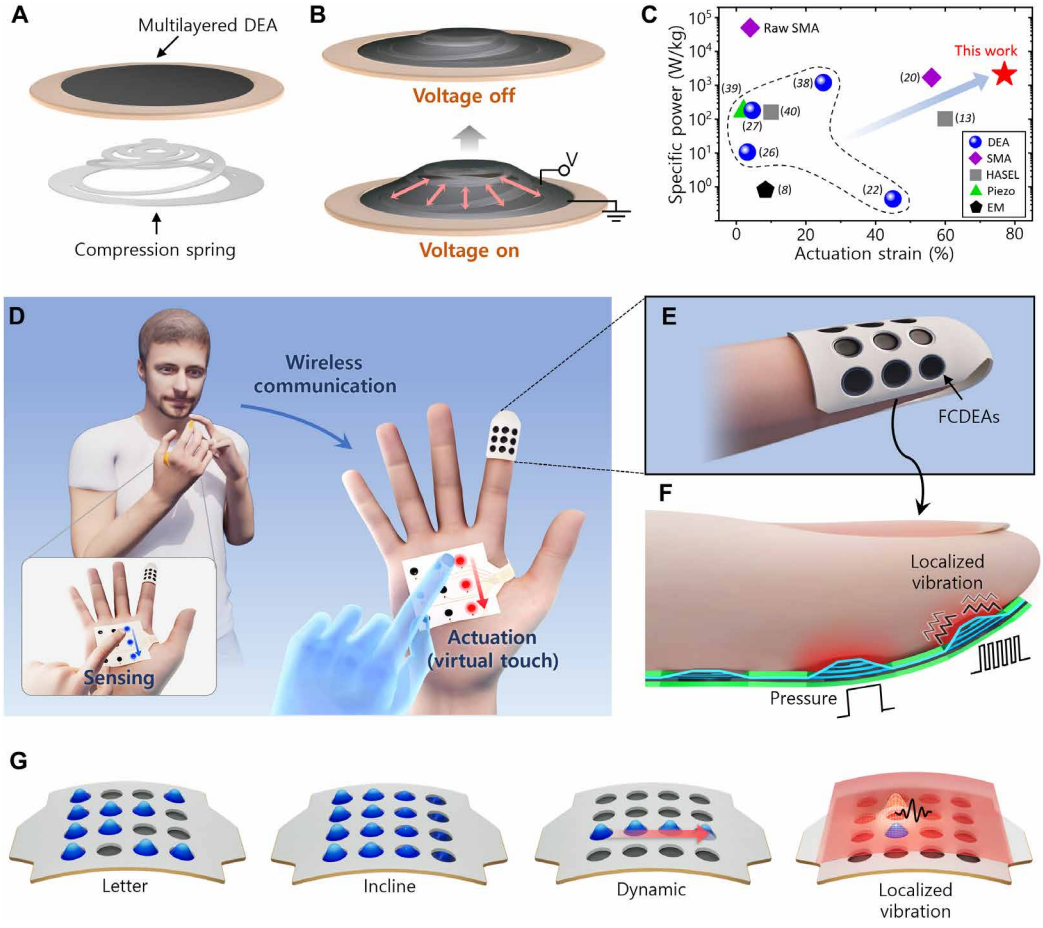

Fig. 1. Schematic of haptic patch. (**A**) Structural configuration and (**B**) operating mechanism of FCDEA that produces large out-of-plane deformation. (**C**) Power-to-weight ratio according to actuation strain of various tactile actuators. (**D**) Scenario of bidirectional tactile communication using haptic patch. (**E**) Schematics of haptic patch enabling conformal contact with skin and (**F**) delivering localized pressure and vibration to skin. (**G**) Illustrations of FCDEA producing morphing surfaces and dynamic tactile information.

letters, three-dimensional (3D) structures, dynamic patterns, and localized vibrations to the user.

Design, operating principle, and characteristic of FCDEA

Before applying wearable tactile interfaces, we first investigated the conversion of the area expansion of the DEA membranes into a linear deformation. Figure 2A illustrates a cross section of the FCDEA, which comprises a prestretched circular DEA membrane coupled with a compression spring that form a conical configuration. In its equilibrium state, the restoring force of the prestretched DEA membrane and deformed compression spring are balanced. Under Maxwell stress, out-of-plane deformation of the FCDEA occurs, as shown in Fig. 2B and movie S2. The initial thickness of the FCDEA plays an important role in converting the area expansion into a vertical actuation strain (see fig. S1 and Supplementary Text). By leveraging the elastic restoring force of the compression spring, the FCDEA achieves high power density while consuming low power. The thin compression spring constructed from spiral flexures allows the FCDEA to produce a relatively high actuation strain compared with other DEAs (see table S1). In addition, the compression spring facilitates generation of stable deformation by preventing buckling owing to its low slenderness ratio and high radial/axial stiffness ratio (*42*). To construct the FCDEA, we selected the 3M 4905 acrylic film as the membrane given its low Young's modulus of 0.4 MPa, high DE constant of 4.53, and high dielectric strength of 25 kV/m (*27*). The DE membrane was biaxially prestretched by a ratio of 4 to enhance the electromechanical properties, such as pull-in voltage and electrical breakdown strength of the DEA (*43*, *44*). The compression spring was made from a 0.1-mm–thick stainless-steel

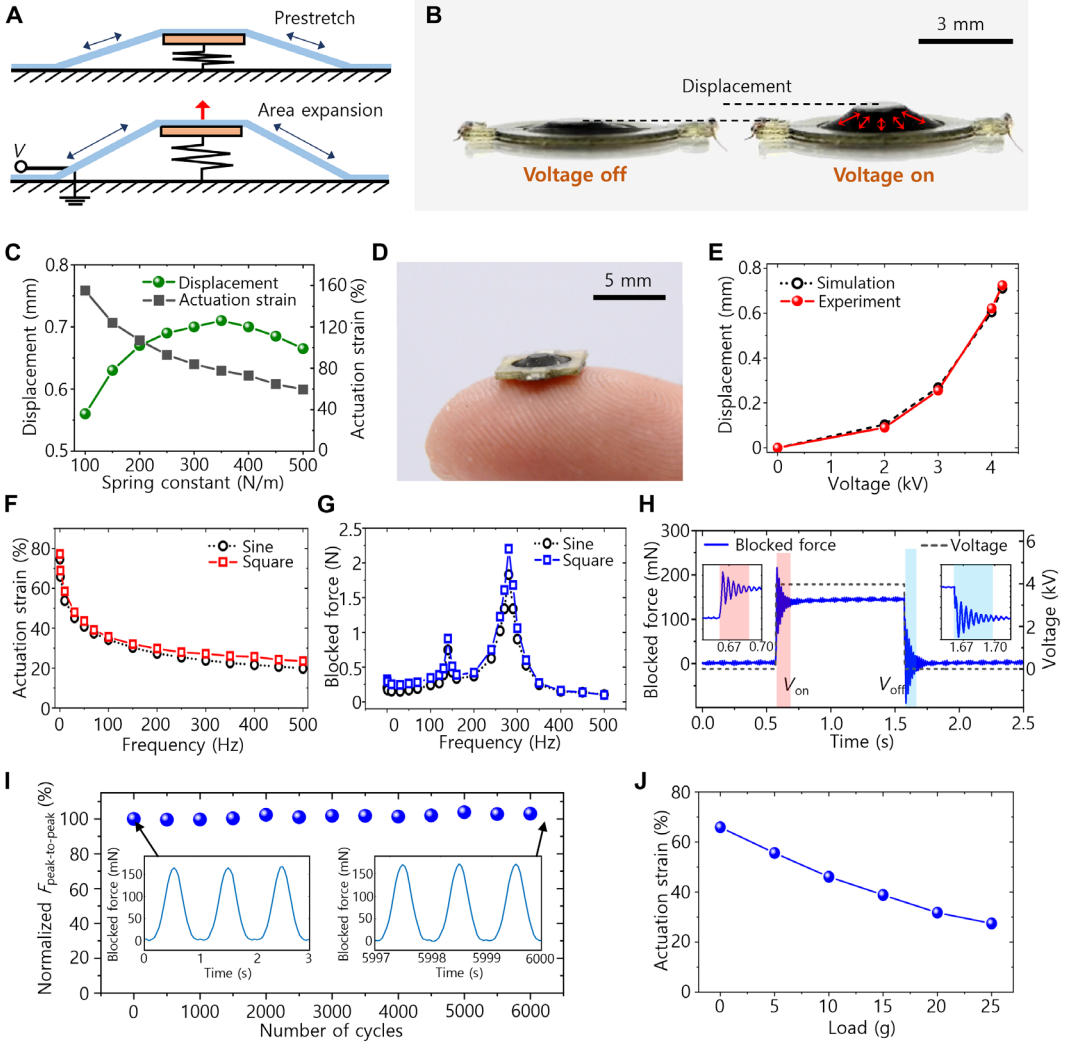

Fig. 2. Operating principles, optimal design, and performance of proposed FCDEA. (**A**) Illustrated FCDEA operation with area strain of DEA under applied voltage *V*. (**B**) Photograph capturing linear out-of-plane deformation. (**C**) Estimated out-of-plane deformation and actuation strain at 1-Hz actuation according to spring constant of compression spring, obtained from the FCDEA dynamic model. (**D**) Photograph of fabricated FCDEA with optimized design. (**E**) Comparison of experimentally measured actuation strain and simulation results according to sinusoidal input voltage at 1 Hz. (**F**) Actuation strain according to operating frequency under sinusoidal and square input at 4.2 kV. (**G**) Blocked force according to operating frequency at 4.2 kV. (**H**) Blocked force profile over time for 4.2-kV square input voltage. (**I**) Change in normalized peak-to-peak blocked force during FCDEA actuation over 6000 deformation-recovery cycles at 1 Hz. (**J**) Actuation strain according to payload under 4.2-kV input voltage at 1 Hz.

sheet through chemical etching. A comprehensive description of the FCDEA fabrication can be found in fig. S2 and Materials and Methods.

Optimizing the equilibrium state between the prestretched DEA with six layers of DE membranes and the compression spring is crucial for attaining a large actuation stroke, which is required to faithfully convey the sensation of a large skin deformation to the users (*20*). Therefore, to maximize the actuation stroke, we optimized the spring constant of the compression spring using an FCDEA dynamic model with the behavior shown in Fig. 2C. Detailed descriptions of the dynamic model can be found in fig. S3 and Supplementary Text. On the basis of the simulation results, we selected the spring constant as 350 N/mm. Notably, the results indicate that the actuation strain of the FCDEA can be further increased by using a compression spring with a smaller spring constant due to the influenced by the initial thickness. The actuation stroke of the FCDEA is also affected by other design parameters of the spring, such as its inner diameter and initial length, which can be further optimized (see fig. S3). Using the finite element method through a simulation in COMSOL Multiphysics software, we designed the spiral flexures of the compression spring with an optimized spring constant (fig. S4 and Materials and Methods). With the optimized design, we fabricated the FCDEA (area of 6 mm by 6 mm, thickness of 1.1 mm, and weight of 32 mg), as shown in Fig. 2D. The mechanical stiffness of the optimized FCDEA (0.65 N mm^{-1}) was similar to the reported mechanical impedance of human fingertip skin (0.6 to 1.2 N mm^{-1}) (*38*).

The optimized FCDEA was characterized by measuring the actuation strain and force. The test setup is detailed in fig. S5 and Materials and Methods. Figure 2E shows that the FCDEA produced a controllable actuation by tuning the input voltage. The dynamic simulation results were validated by comparing them with experimental results. Figure 2F shows the actuation strain profile of the FCDEA according to the actuation frequency at an input voltage of 4.2 kV. The FCDEA could operate across a broad frequency range (0.1 to 500 Hz), achieving a maximum actuation strain of 77.1% (corresponding to an 848.8-μm actuation stroke) at 0.1 Hz, with a rapid response time below 50 ms and a bandwidth of 12 Hz (fig. S6). The FCDEA could produce a durable and stable peak-to-peak actuation strain with a small deviation (<3%) even during continuous operation for 6000 s at both low (1 Hz) and high (100 Hz) frequency operation, as shown fig. S6. However, we observed the output displacement gradually drifting from its equilibrium position due to the inherent viscoelasticity of acrylic films (fig. S6) (*45*).

Figure 2G shows that the FCDEA generates a maximum peak-to-peak blocked force of 2.2 N at its resonance frequency of 280 Hz with a quasi-static blocked force reaching up to 200 mN and a response time below 50 ms (fig. S7). The resonance frequency of the FCDEA closely aligned with the frequency band to which the skin is most sensitive (100 to 300 Hz). The blocked force profile showed two peaks at 140 and 280 Hz owing to the Maxwell stress applied to DEA being proportional to the square of the input voltage (see Materials and Methods for details) (*42*). We hypothesize that this resonance frequency likely originates from the compression spring within the FCDEA. We also observed that the resonance frequency of the FCDEA shifts under different applied preload conditions (fig. S7). Figure 2H shows that the time response of the FCDEA blocked force driven by a 0.5-Hz square input voltage, exhibiting oscillation similar to a typical mass-spring-damper system. This oscillation led the FCDEA to produce a higher blocked force under a square signal than under a sinusoidal signal. To investigate the batch-to-batch variation of FCDEAs, we fabricated five FCDEAs with the same design and compared their measured blocked force under a sinusoidal input signal at 280 Hz (fig. S7). Results showed that fabrication defects, likely caused by tiny air bubbles trapped during the stacking process, led to variation in the blocked force of up to 26%. We validated that the FCDEA maintained stable output forces during continuous operation for 6000 s with a deviation of 3.8% at 1 Hz and 11.2% at 280 Hz (Fig. 2I and fig. S7). Despite its weight of 32 mg, the FCDEA could lift 25 g, which is more than 780 times its own weight, with an actuation strain of 27.4%, corresponding to a displacement of 199 μm, as shown in Fig. 2J and movie S3. Hence, the maximum power density (power-to-weight ratio) and specific energy density of FCDEA were calculated to be 2.09 kW/kg and 1.56 J/kg, respectively (see Materials and Methods for details). For the calculation, the weight of the FCDEA included all the passive components, such as frames (11 mg) and electrical connections (5 mg). Therefore, the power density and specific energy density of the FCDEA may be increased by reducing the weight of passive components. To verify the effectiveness of FCDEAs for tactile feedback, we calculated the skin deformation caused by FCDEA using a mechanical impedance model of the skin and the measured performance of the FCDEAs (see fig. S8) (*38*). The results shown indicated that the estimated skin deformation cause by FCDEA exceeded the detection thresholds of the fingertip by more than 30 times (up to 262 times at 280 Hz) but was a few times higher than the forearm (up to 26 times at 280 Hz) across the entire frequency range (30 to 280 Hz) (*36*). Considering that the forearm is one of the most insensitive parts of the body to touch, these results reveal that FCDEAs have ability to provide perceivable tactile feedback to various body parts (*36*). The FCDEA exhibited a power consumption of 0.89 mW at 1-Hz actuation and 56.87 mW at 280-Hz actuation (fig. S9 and Materials and Methods). The increase in power consumption at a high operating frequency was due to the dielectric loss properties of the acrylic membrane (*46*).

FCDEA array for wearable haptic patch

We constructed a 4 by 4 FCDEA array comprising a multilayered DEA array, a compression spring array, and a flexible PCB, as shown in Fig. 3A. To obtain a dense array, the actuators were spaced at a pitch of 6 mm. A thin insulating membrane (3M F9473PC) was incorporated to ensure user safety and secure strong adhesion to the skin. The fabrication of the FCDEA array is described in fig. S10 and Materials and Methods. The flexible thin FCDEA array allowed independent control of each actuator at a high speed (Fig. 3B and movie S4). By controlling each FCDEA independently, the array allowed to dynamically express English letters (Fig. 3C), the topology of 3D structures (Fig. 3D), and various dynamic patterns (Fig. 3E). In addition, the FCDEA array could produce both single- and multipoint localized vibrations on the surface, as shown in Fig. 3 (F to H) and movie S5.

Using a 3 by 3 FCDEA array, we designed a thin flexible haptic patch for a fingertip and the palm of the hand, as shown in Fig. 4 (A and B). The two-point threshold of the fingertip is 2 to 3 mm under static stimuli (*47*) and increases to 5.1 mm under vibrational stimuli (*48*). The two-point threshold of the palm is 10 to 12 mm (*47*). Therefore, we designed a haptic patch with a pitch of 6 mm for the fingertip and 12 mm for the palm, aligning closely with the two-point thresholds. The entire haptic patch was extremely thin, flexible, and lightweight (0.3 g), enabling conformal contact with the skin. Figure 4C shows the block diagram of the control circuit module. As

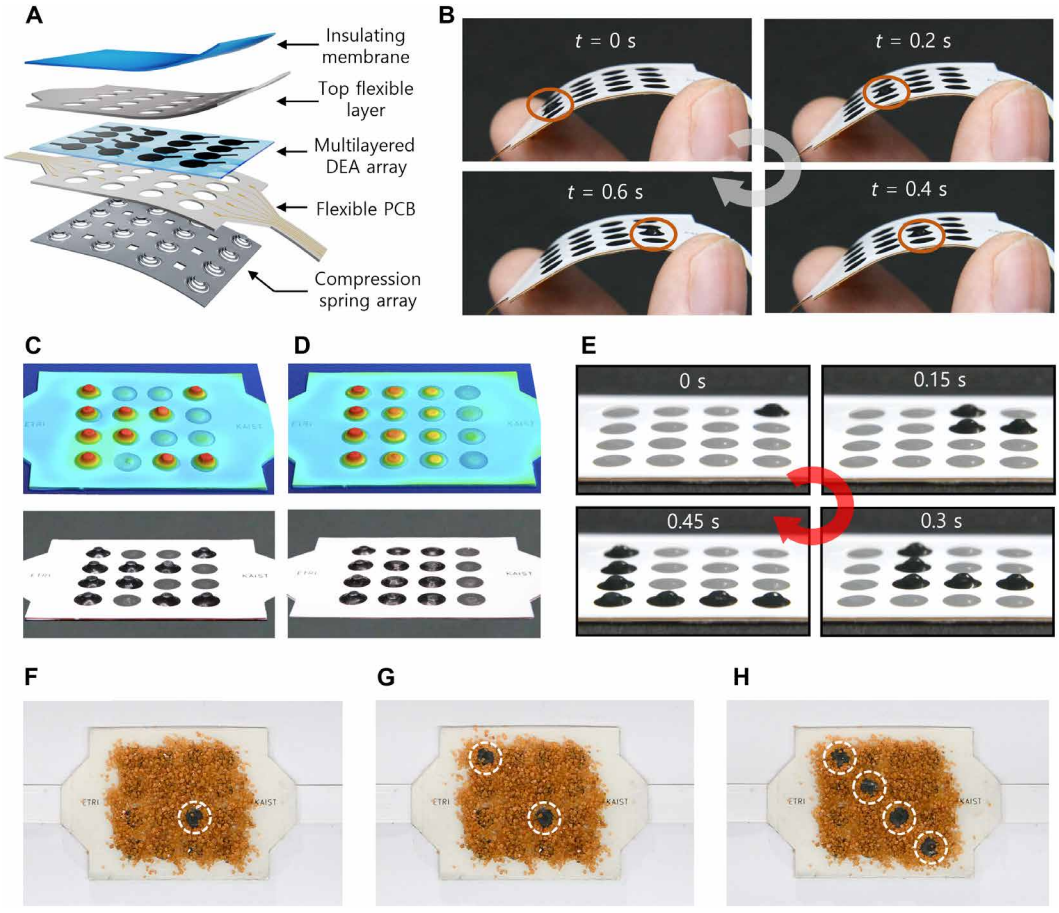

Fig. 3. Design and performance of FCDEA array. (**A**) Exploded view of FCDEA array. (**B**) Flexible thin FCDEA array generating large deformation at high speed. Photographs with 3D profiler images of FCDEA array expressing (**C**) letter K and (**D**) contour. (**E**) Photograph of FCDEA array producing dynamic pattern at high speed. Photographs of FCDEA array producing localized vibration at (**F**) single and (**G** and **H**) multiple points.

shown in Fig. 4D, the control circuit module consisted of a high-voltage module, a microcontroller unit (MCU) with a built-in Bluetooth module, and a small 1000-mAh rechargeable lithium-ion battery. The high-voltage signal was controlled and independently delivered to each of the nine FCDEAs using an optocoupler array. The voltage intensity could be modulated by a high-voltage DC/DC converter module from 0 to 4 kV. The control circuit module was sufficiently compact and lightweight (47 g) to be comfortably attached to the arm. The details of the circuit design are shown in fig. S11 and Materials and Methods. To ensure safe interaction, the control circuit module limited the current of the high-voltage source to 100 μA, and additional 20-megohm resistors were connected to the FCDEAs for short-circuit protection. Furthermore, the user had contact with an insulating membrane over the ground electrodes to ensure safety.

Wireless tactile interaction

The proposed haptic patch synchronized tactile information to the user's hand in a VR environment (Fig. 4E and Materials and Methods). As depicted in Fig. 4F and movie S6, the fingertip haptic patch delivered feedback related to the contact geometry, such as an edge or corner of a virtual object, to the user in real time. When the user interacted with a virtual object, the contact geometry of the object was wirelessly transferred to the device and reproduced tactile cues by controlling each actuator unit. In addition, the fingertip haptic patch could render the texture of a virtual object using vibration.

To investigate the ability of a user to recognize dynamic haptic reproduction from the fabricated haptic patches, various user tests were conducted, as shown in Fig. 4G. First, we measured the actuation voltage thresholds of the FCDEA at two operating frequencies (1 and 280 Hz) using a square signal across three body parts, including fingertip, palm of the hand, and forearm (see fig. S12 and Materials and Methods). As shown in Fig. 4H, results indicate that FCDEA can deliver both low-frequency tactile feedback and high-frequency vibration feedback at all tested body parts. Consistent with reported detection thresholds, the fingertip exhibited the lowest voltage thresholds (*36*). Then, we investigated the ability of the participants to recognize various dynamic patterns at their fingertip and palm (see Materials and Methods). During the test, the input voltages of 1.2 and 4 kV were applied to the fingertip and the palm, respectively, considering vibrotactile sensitivity according to body parts shown in the test results of the actuation voltage thresholds. Each actuator was operated at 280 Hz during pattern presentation. As a result, the fingertip feedback was recognized with more than 98% accuracy (Fig. 4I), and the palm feedback was recognized with more than 97% accuracy (fig. S12).

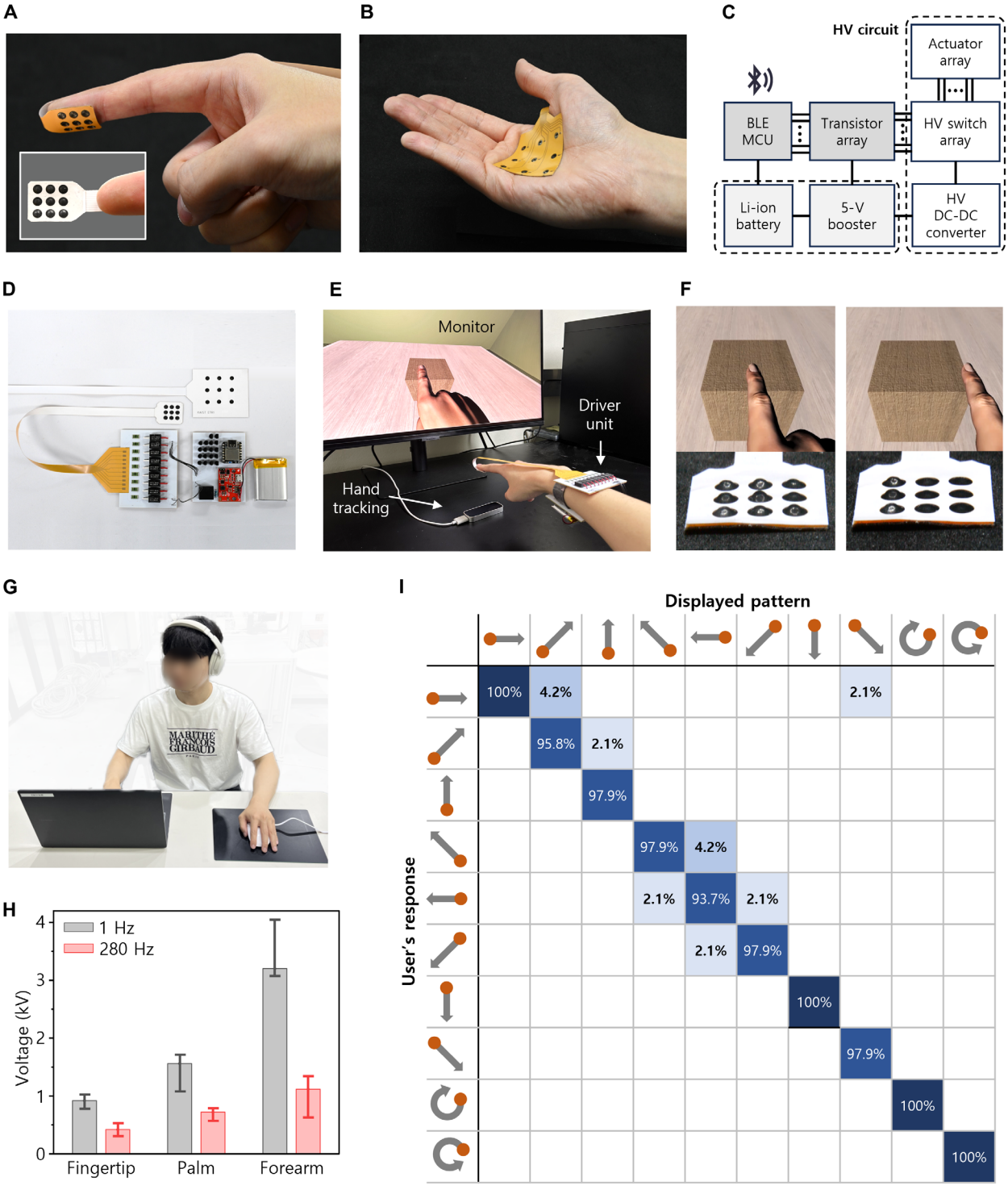

Fig. 4. Wireless tactile communication using haptic patch and user tests. Thin flexible haptic patch for (**A**) fingertip and (**B**) palm of the hand. (**C**) Circuit diagram of tactile feedback module. HV, High Voltage; BLE, Bluetooth Low Energy. (**D**) Photograph of haptic patches for fingertip and palm along with control circuit module. (**E**) Test setup and (**F**) VR scenario with synchronized contact geometry and texture of virtual box. The geometry was conveyed to the user through tactile feedback. (**G**) Setup for user test. (**H**) Measured actuation voltage thresholds of the FCDEA at two frequencies (1 and 280 Hz) across fingertip, palm, and forearm. Error bars indicate minimum and maximum values of the data. (**I**) Confusion matrix obtained from user testing fingertip haptic patch.

We then tested the capability of frequency discrimination. During each trial, two different tactile stimuli with different frequencies (1, 3, 10, 30, or 120 Hz) were presented one at a time in random order over 3 s. The participants were asked to identify the stimulus with the higher perceived frequency. A total of 40 trials were presented to each participant. Results in fig. S12 show that all participants discriminated the higher-frequency stimulus with 100% accuracy. This result demonstrated the ability of the participants to discriminate complex dynamic patterns with various vibration frequencies.

Last, we evaluated texture discrimination. Four tactile renderings of surface texture were created, and two different renderings were presented one at a time in random order during each test. The participants were asked to identify the rougher texture stimulation. A total of 24 trials were conducted per participant. The participants discriminated the rougher textures with more than 98% accuracy, as shown in fig. S12.

Tactile sensing capability for wireless tactile communication

In addition to the tactile actuators, tactile sensing capabilities are desirable in wearable systems to perform bidirectional tactile communication (*8*). Integrating tactile actuators and sensors enables the synchronization and transmission of tactile sensations from one user to another. To establish wireless tactile communication, we integrated the FCDEA array with the flexible sensor array, as shown in Fig. 5A. The flexible sensor array consisted of a 3 by 3 reflective photomicrosensor (Omron EE-SY 199) embedded in a flexible PCB. Figure 5B shows the sensing principle of measuring the contact force. An applied contact pressure deformed the FCDEA, resulting in a decrease in the distance between the FCDEA and sensor. The reflective photomicrosensor quickly measured this distance. Figure 5C shows the circuit block diagram of the tactile sensing mode, where the outputs of the sensors in the array were collected using a multiplexer. Figure 5D shows the relationship between the external load force and tactile sensing voltage from the photomicrosensor using the test setup shown in fig. S13. The sensors exhibited a high linearity with a coefficient of determination (R^2) of 0.995 and sensitivity of 2.55 V/N. In a cycling performance test with 10,000 cycles, the sensor produced a stable sensing performance with a small deviation of 0.81%, as shown in fig. S13B. By integrating a 3 by 3 sensor array into the actuator array, we validated the tactile sensing performance. When a particular actuator was pressed by a finger, the corresponding sensor generated the output signal in real time, as shown in Fig. 5E and movie S7. In addition, movie S7 shows that the sensor array had a negligible response to mechanical bending, making it suitable

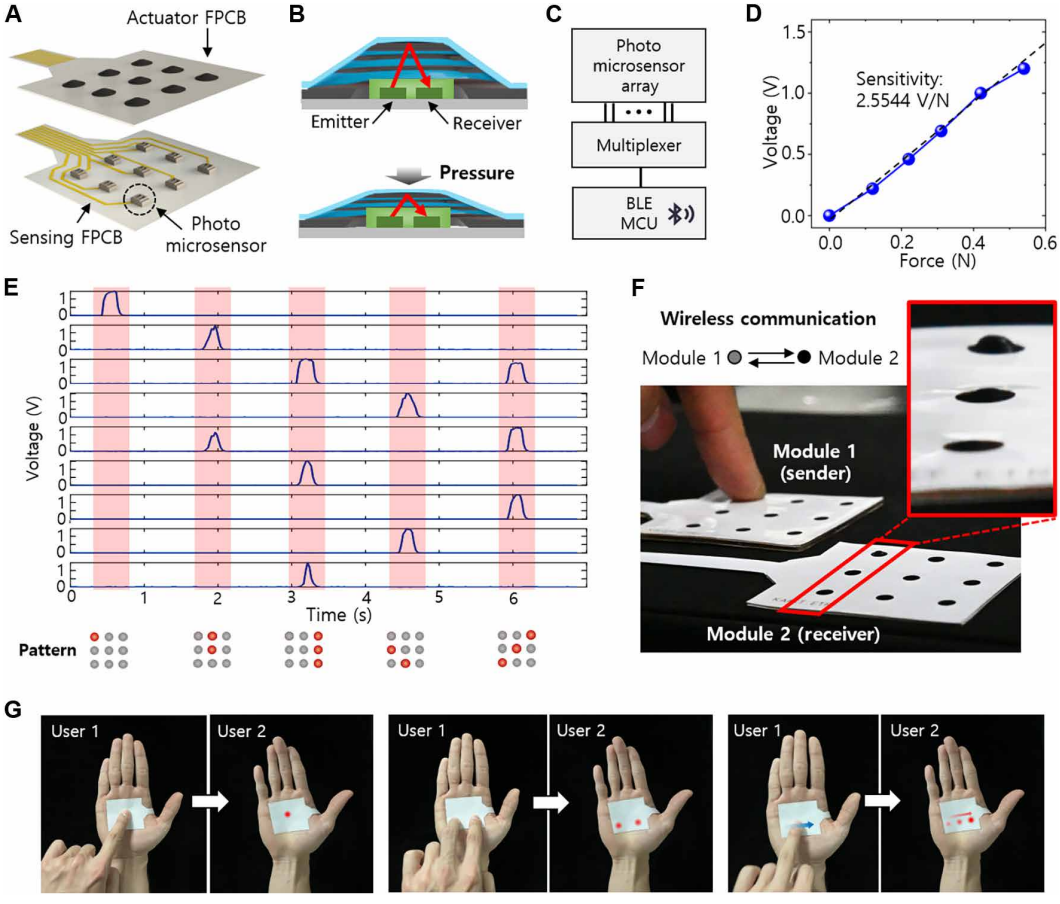

Fig. 5. Haptic patch with tactile sensing capability. (**A**) Exploded view schematic of self-sensing haptic patch combining FCDEA and sensor arrays. (**B**) Principle of FCDEA tactile sensing using photomicrosensor. (**C**) Circuit diagram of tactile sensing module. (**D**) Sensor output according to applied force. (**E**) Sensor array outputs over time with various tactile patterns indicating locations (red dots) pressed by user's finger. (**F** and **G**) Photographs of wireless tactile communication between two haptic patches in real time integrating tactile sensing and feedback.

for wearable applications. Figure 5F and movie S8 show that pressure information could be transferred from one haptic patch to another in real time through wireless communication.

DISCUSSION

We introduce a thin flexible haptic patch conformally attached to the skin that can deliver tactile feedback to a large area by exploiting a dense array of thin soft FCDEAs. The proposed FCDEA is distinguished from previous tactile actuators by its flexibility, high actuation strain, high output power density, fast response time, light weight, and thin form factor. The proposed haptic patch can enhance immersive experiences in VR and AR applications by conveying contact geometries or textures of virtual objects. By integrating FCDEA and tactile sensor arrays, tactile information, such as touching sensation or dynamic patterns, can be encoded and transmitted between users or in VR/AR environments through wireless communication. The haptic patch can be used in various fields, such as entertainment, social media, education, and remote robot control.

At the current stage of development, the most challenging issue of our tactile solution is the use of high-voltage sources, but the low current and insulating layer can ensure user safety. Future work will be focused on reducing the driving voltage by optimizing the DE material and reducing the thickness of the DE membrane to the submicron scale using the Langmuir-Schaefer method (*49*) or pad printing (*50*). By reducing the driving voltage below 500 V, the user safety may be improved, and the driving electronics may be miniaturized (*15*, *23*). In addition, the output power and power consumption can be further enhanced by replacing the DE material from acrylic elastomer to silicones owing to their low mechanical and electrical loss at high frequencies (*31*, *32*, *46*). We also believe that batch-to-batch variations in FCDEAs could be further minimized by using DE materials that do not require prestretching, thereby simplifying the fabrication process (*51*). Although the FCDEA was used for tactile actuators, we believe that numerous other applications are feasible, including soft robotics such as micromanipulators, microgrippers, and biomimetic robots, given the high actuation strain and power density of the FCDEA.

MATERIALS AND METHODS

FCDEA fabrication

The FCDEA fabrication is depicted in fig. S2. First, the DE membrane (3M VHB 4905) was biaxially prestretched at a ratio of 4 and bonded to a thin frame with a thickness of 100 μm (FR4 plate) and an inner diameter of 4 mm. Multiwalled carbon nanotubes were coated to both sides of the membrane as compliant electrodes. Aluminum tape with a thickness of 30 μm was attached for electrical connection. By stacking the prestretched DE membrane with compliant electrodes on both sides six times, a multilayered DEA was obtained. A thin 80-μm passive membrane was integrated between the DE membranes to maintain pretension. Subsequently, the compression spring was fabricated as follows (fig S2, D to I). The spiral flexure was prepared through chemical etching of a stainless-steel (SUS304) sheet with a thickness of 0.1 mm. To shape a deformed compression spring from the spiral flexure, a heat process was applied. The spiral flexure was fitted between two frames, causing deformation of 2.5 mm at its center. For accurate center alignment, the layers were aligned using dowl pins. The spiral flexure was transformed into a deformed compression spring after heating at 380°C for 6 hours using a hot plate. The compression spring was further coated with polyurethane spray (20 μm thick) to insulate the surface and smoothen the edges for enhanced stability. The thickness of the fabricated compression spring was 2.5 mm. The FCDEA fabrication was done by combining the multilayered DEA and compression spring.

Computational simulation

A numerical analysis of the spiral flexure was conducted using the finite element method with COMSOL software. The spiral flexure was designed with various spiral gaps and slot widths. During simulation, vertical pressure was applied at the center of the spiral flexure, and the outer surface of the spiral flexure was fixed. Simulation results showed that the deformation had a linear relationship with the applied force, as shown in fig. S4C. The spring constant of the spiral flexure was estimated as the ratio between the applied force and deformation in the simulation. Results in fig. S4D show that the spring constant has a negative linear relationship with a slot width. The spiral flexure with a slot gap of 0.25 mm and the slot width of 0.125 mm has a spring constant of 350 N/m, which is an optimized value determined during the dynamic simulation. The estimated and measured spring constants are shown in fig. S4F. The results indicated that both the spiral flexure and the compression spring made of spiral flexures exhibit similar spring properties to the simulated results. The test setup of measuring the spring constant of the fabricated compression spring is shown in fig. S4E.

Performance test

The FCDEA deformation during a dynamic repeatability test was measured using a laser scanning vibrometer (Polytec PSV-500). A two-degree-of-freedom motorized linear stage (Optic Focus MOXYZ-02) was used to guarantee precise actuator alignment. During the test, the input voltage was generated by a data acquisition device (NI USB-6351) with various frequencies and waveforms and amplified by a high-voltage amplifier (Matsusada AMJ-4B10). The 3D shape of the deformed FCDEA unit and array were captured by a 3D profiler (KEYENCE VR-3000) (Fig. 3 and fig. S6). The blocked force of the FCDEA was measured by attaching the central point of actuator to a load cell (Dacell UMI-G500). To minimize the influence of the load cell's resonance frequency, we selected a load cell with a high resonance frequency of approximately 3.5 kHz. During the test, a small preload of less than 10 mN is applied by precisely controlling the position of the load cell using a motorized linear stage. Similar to the displacement measurement test, force data were collected by a NI USB-6351 data acquisition device, and a three-degree-of-freedom motorized linear stage (Optic Focus MOXYZ-02) was used to guarantee precise actuator alignment.

Two peaks of the blocked force

The input voltage (V) of the FCDEA was a sinusoidal signal with an offset, which can be expressed as

$$V = \frac{A}{2}[1 - \cos(2\pi ft)] \quad (1)$$

where A is the voltage magnitude, f is the operating frequency, and t is the time. Then, the applied Maxwell stress (p) of the DEA under applied voltage V can be expressed as

$$p = \varepsilon_0\varepsilon_r\left(\frac{V}{t_{DEA}}\right)^2 = \frac{A^2\varepsilon_0\varepsilon_r}{8t_{DEA}^2}[1 - 4\cos(2\pi ft) + \cos(4\pi ft)] \quad (2)$$

where ε_0 is the permittivity of free space, ε_r is the relative permittivity of the DE membrane, and t_{DEA} is the thickness of the DE membrane. Equation 2 shows that the Maxwell stress of DEA includes components at both operating frequency *f* and its harmonic *2f*. Notably, the magnitude of *2f* component is one-fourth that of the *f* component. We believe that this explains the presence of two peaks in the measured blocked force profile, which is also observed in other cone DEAs (*27*, *52*).

Power density and specific energy calculation

Power density of the FCDEA was estimated as

$$P = \frac{F\delta f}{2m} \quad (3)$$

where *P* is the power density of the FCDEA, *m* is the mass of the FCDEA, *F* is the blocked force, δ is the output displacement, and *f* is the operating frequency (*39*). The FCDEA weighing 32 mg had a maximum power density of 2.09 kW/kg at 280 Hz (blocked force of 1.83 N and displacement of 0.26 mm). The specific energy of the DEA was calculated from payload test results (Fig. 2J).

Power consumption of FCDEA

The power consumption of the FCDEA was measured by recording the voltage and current of the 4-kV sinusoidal input voltage at 1 and 280 Hz using a high-voltage probe (Keysight N2891A), data acquisition device, and low-current preamplifier (Stanford Research Systems SR570). The maximum current of the FCDEA was 1.4 μA at 1 Hz and 148 μA at 280 Hz under a 4-kV sinusoidal input voltage, as shown in fig. S9.

Haptic patch fabrication

The haptic patch consisted of an FCDEA array for tactile feedback and photomicrosensor array for tactile sensing. The haptic patch fabrication is depicted in fig. S10. To create the FCDEA array, a thin flexible PCB (80 μm thick) was prepared with nine holes inside (diameter of 4 mm and pitch of 6 mm). Similar to the fabrication of an FCDEA unit, the DE (3M VHB 4905) was prestretched, and carbon nanotubes were coated onto it using a patterned mask. To obtain reliable electrical interconnects, a 30-nm–thick gold layer was sputtered on the carbon nanotube electrode connection region using a sputter coater (Q300T T Plus) (*53*). This procedure was repeated six times to form stacked DEAs. After stacking the DEAs, we punctured the DEA electrode connection regions and filled the hole with conductive silver epoxy (*53*). A thin top flexible layer made of polyimide with nine holes was attached to the stacked DEAs. The fabrication of the FCDEA array was finished by combining the multilayered DEA array with the prepared compression spring array. The sensor array was prepared by soldering nine photomicrosensors (Omron EE-SY199) on the flexible PCB. By combing the FCDEA and sensor arrays with a 500-μm-thick spacer (3M VHB 4905), the haptic patch was complete.

Circuit design

The driver circuit was built on a PCB with a thickness of 1 mm. The driver circuit was composed of a high-voltage DC/DC converter (HVM Technology UMHV0540), high-voltage optocouplers (HVM Technology OPTO-150), transistors (PN222A), resistors, DC/DC converter module (from 3.3 to 5 V), and MCU with a built-in Bluetooth Low Energy module (Seeed Studio XIAO NRF52840). All the electronic components were soldered on the exposed pads or pin holes of the PCB. A compact (12.7 mm by 12.7 mm by 12.7 mm) high-voltage DC/DC converter generated 0 to 4 kV with a power output of 500 mW, limiting the maximum current to 125 μA. Transistors amplified the current of the digital outputs from the MCU to switch the high voltage using the optocoupler array. The optocoupler array was connected to the actuator array for charging and discharging the actuators at high speed. For the sensing array, the photomicrosensor array was connected to a 16-channel multiplexer switch (CD74HCT4067MG4).

Virtual environment

A VR environment was created using Unity3D with hand tracking enabled by an Ultraleap Leap Motion controller. When a user contacted a virtual object, Unity3D generated collision detection points on a hand model. The collision information was transmitted to the control unit via wireless communication and synchronized to the tactile feedback.

Actuation voltage threshold test

The perception studies on human volunteers were approved by the Institutional Review Board of Korea Advanced Institute of Science and Technology (KH-2023-249). The device was mounted on the fingertip, palm, and forearm of six participants, as shown in fig. S12. To eliminate auditory cues, every participant wore headphones during the test, as shown in Fig. 4G. We used a descending transformed 1-up-2-down double staircase procedure to determine 70.7% detection thresholds for perceiving tactile feedback from the actuator. Square signals at 1 and 280 Hz were applied, and participants were asked whether they could feel the tactile feedback. The test began with an easily perceived amplitude, which gradually reduced until the participants no longer felt the sensation. The intensity of the actuator was then increased, until participants responded that they perceived the tactile feedback. Then, we applied the same signal to the participants, and if the participant's response was consistent for both two signals, the intensity was further decreased. This procedure continued until eight reversal responses were recorded, and the detection threshold was calculated as the average of the last three reversals.

Dynamic pattern discrimination test

The perception studies on human volunteers were approved by the Institutional Review Board of Korea Advanced Institute of Science and Technology (KH-2023-249). The device was mounted on a table, and the users placed their finger and palm on it. The user test was conducted with 12 participants. Every participant wore headphones to filter any sounds emitted by the actuator, as shown in Fig. 4G. To make conformal contact, the device was mounted on a curved surface, as shown in fig. S12. First, we produced 10 dynamic patterns to a fingertip and the palm of the user. Before the test, each pattern was presented once to every participant for training. After training, the patterns were presented once at a time in random order, and every participant was asked to recognize the presented pattern. Each of the 10 dynamic patterns was presented four times in random order. During pattern presentation, each actuator was operated for 1 s.

Supplementary Materials

The PDF file includes:

Supplementary Text
Figs. S1 to S13
Table S1
Legends for movies S1 to S8
References

Other Supplementary Material for this manuscript includes the following:
Movies S1 to S8

REFERENCES AND NOTES

1. J. K. Gibbs, M. Gillies, X. Pan, A comparison of the effects of haptic and visual feedback on presence in virtual reality. *Int. J. Hum. Comput. Stud.* **157**, 102717 (2022).
2. M. Gopakumar, G.-Y. Lee, S. Choi, B. Chao, Y. Peng, J. Kim, G. Wetzstein, Full-colour 3D holographic augmented-reality displays with metasurface waveguides. *Nature.* **629**, 791–797 (2024).
3. T.-H. Yang, J. R. Kim, H. Jin, H. Gil, J.-H. Koo, H. J. Kim, Recent advances and opportunities of active materials for haptic technologies in virtual and augmented reality. *Adv. Funct. Mater.* **31**, 2008831 (2021).
4. HaptX Gloves G1 | Realistic touch for the enterprise metaverse; https://haptx.com.
5. W. Wang, Y. Jiang, D. Zhong, Z. Zhang, S. Choudhury, J.-C. Lai, H. Gong, S. Niu, X. Yan, Y. Zheng, C.-C. Shih, R. Ning, Q. Lin, D. Li, Y.-H. Kim, J. Kim, Y.-X. Wang, C. Zhao, C. Xu, X. Ji, Y. Nishio, H. Lyu, J. B.-H. Tok, Z. Bao, Neuromorphic sensorimotor loop embodied by monolithically integrated, low-voltage, soft e-skin. *Science* **380**, 735–742 (2023).
6. W. Gao, S. Emaminejad, H. Y. Y. Nyein, S. Challa, K. Chen, A. Peck, H. M. Fahad, H. Ota, H. Shiraki, D. Kiriya, D.-H. Lien, G. A. Brooks, R. W. Davis, A. Javey, Fully integrated wearable sensor arrays for multiplexed in situ perspiration analysis. *Nature* **529**, 509–514 (2016).
7. K. Yao, J. Zhou, Q. Huang, M. Wu, C. K. Yiu, J. Li, X. Huang, D. Li, J. Su, S. Hou, Y. Liu, Y. Huang, Z. Tian, J. Li, H. Li, R. Shi, B. Zhang, J. Zhu, T. H. Wong, H. Jia, Z. Gao, Y. Gao, Y. Zhou, W. Park, E. Song, M. Han, H. Zhang, J. Yu, L. Wang, W. J. Li, X. Yu, Encoding of tactile information in hand via skin-integrated wireless haptic interface. *Nat. Mach. Intell.* **4**, 893–903 (2022).
8. D. Li, J. Zhou, K. Yao, S. Liu, J. He, J. Su, Q. Qu, Y. Gao, Z. Song, C. Yiu, C. Sha, Z. Sun, B. Zhang, J. Li, L. Huang, C. Xu, T. H. Wong, X. Huang, J. Li, R. Ye, L. Wei, Z. Zhang, X. Guo, Y. Dai, Z. Xie, X. Yu, Touch IoT enabled by wireless self-sensing and haptic-reproducing electronic skin. *Sci. Adv.* **8**, eade2450 (2022).
9. D. Li, J. He, Z. Song, K. Yao, M. Wu, H. Fu, Y. Liu, Z. Gao, J. Zhou, L. Wei, Z. Zhang, Y. Dai, Z. Xie, X. Yu, Miniaturization of mechanical actuators in skin-integrated electronics for haptic interfaces. *Microsyst. Nanoeng.* **7**, 85 (2021).
10. X. Yu, Z. Xie, Y. Yu, J. Lee, A. Vazquez-Guardado, H. Luan, J. Ruban, X. Ning, A. Akhtar, D. Li, B. Ji, Y. Liu, R. Sun, J. Cao, Q. Huo, Y. Zhong, C. M. Lee, S. Y. Kim, P. Gutruf, C. Zhang, Y. Xue, Q. Guo, A. Chempakasseril, P. Tian, W. Lu, J. Y. Jeong, Y. J. Yu, J. Cornman, C. S. Tan, B. H. Kim, K. H. Lee, X. Feng, Y. Huang, J. A. Rogers, Skin-integrated wireless haptic interfaces for virtual and augmented reality. *Nature* **575**, 473–479 (2019).
11. Y. H. Jung, J.-Y. Yoo, A. Vázquez-Guardado, J.-H. Kim, J.-T. Kim, H. Luan, M. Park, J. Lim, H.-S. Shin, C.-J. Su, R. Schloen, J. Trueb, R. Avila, J.-K. Chang, D. S. Yang, Y. Park, H. Ryu, H.-J. Yoon, G. Lee, H. Jeong, J. U. Kim, A. Akhtar, J. Cornman, T.-i. Kim, Y. Huang, J. A. Rogers, A wireless haptic interface for programmable patterns of touch across large areas of the skin. *Nat. Electron.* **5**, 374–385 (2022).
12. E. Leroy, R. Hinchet, H. Shea, Multimode hydraulically amplified electrostatic actuators for wearable haptics. *Adv. Mater.* **32**, 2002564 (2020).
13. E. Leroy, H. Shea, Hydraulically amplified electrostatic taxels (HAXELs) for full body haptics. *Adv. Mater. Technol.* **8**, 2300242 (2023).
14. S. Chen, Y. Chen, J. Yang, T. Han, S. Yao, Skin-integrated stretchable actuators toward skin-compatible haptic feedback and closed-loop human-machine interactions. *Npj Flex. Electron.* **7**, 1 (2023).
15. V. Shen, T. Rae-Grant, J. Mullenbach, C. Harrison, C. Shultz, "Fluid reality: High-resolution, untethered haptic gloves using electroosmotic pump arrays," in *Proceedings of the 36th Annual ACM Symposium on User Interface Software and Technology* (ACM, 2023), pp. 1–20.
16. M. Zhu, Z. Sun, Z. Zhang, Q. Shi, T. He, H. Liu, T. Chen, C. Lee, Haptic-feedback smart glove as a creative human-machine interface (HMI) for virtual/augmented reality applications. *Sci. Adv.* **6**, eaaz8693 (2020).
17. H. Jin, Y. Kim, W. Youm, Y. Min, S. Seo, C. Lim, C.-H. Hong, S. Kwon, G. Park, S. Park, H. J. Kim, Highly pixelated, untethered tactile interfaces for an ultra-flexible on-skin telehaptic system. *Npj Flex. Electron.* **6**, 82 (2022).
18. H. A. Sonar, A. P. Gerratt, S. P. Lacour, J. Paik, Closed-loop haptic feedback control using a self-sensing soft pneumatic actuator skin. *Soft Robot.* **7**, 22–29 (2020).
19. N. Morita, A. Ichijo, M. Konyo, H. Kato, K. Sase, H. Nagano, S. Tadokoro, Wearable high-resolution haptic display using suction stimuli to represent cutaneous contact information on finger pad. *IEEE Trans. Haptics* **16**, 687–694 (2023).
20. D. Kim, B. Kim, B. Shin, D. Shin, C.-K. Lee, J.-S. Chung, J. Seo, Y.-T. Kim, G. Sung, W. Seo, S. Kim, S. Hong, S. Hwang, S. Han, D. Kang, H.-S. Lee, J.-S. Koh, Actuating compact wearable augmented reality devices by multifunctional artificial muscle. *Nat. Commun.* **13**, 4155 (2022).
21. I. M. Koo, K. Jung, J. C. Koo, J.-D. Nam, Y. K. Lee, H. R. Choi, Development of soft-actuator-based wearable tactile display. *IEEE Trans. Robot.* **24**, 549–558 (2008).
22. S. Mun, S. Yun, S. Nam, S. K. Park, S. Park, B. J. Park, J. M. Lim, K.-U. Kyung, Electro-active polymer based soft tactile interface for wearable devices. *IEEE Trans. Haptics* **11**, 15–21 (2018).
23. X. Ji, X. Liu, V. Cacucciolo, Y. Civet, A. El Haitami, S. Cantin, Y. Perriard, H. Shea, Untethered feel-through haptics using 18-μm thick dielectric elastomer actuators. *Adv. Funct. Mater.* **31**, 2006639 (2021).
24. F. Carpi, G. Frediani, D. D. Rossi, Hydrostatically coupled dielectric elastomer actuators. *IEEE ASME Trans. Mechatron.* **15**, 308–315 (2009).
25. H. S. Lee, H. Phung, D.-H. Lee, U. K. Kim, C. T. Nguyen, H. Moon, J. C. Koo, H. R. Choi, Design analysis and fabrication of arrayed tactile display based on dielectric elastomer actuator. *Sens. Actuator A Phys.* **205**, 191–198 (2014).
26. H. Zhao, A. M. Hussain, A. Israr, D. M. Vogt, M. Duduta, D. R. Clarke, R. J. Wood, A wearable soft haptic communicator based on dielectric elastomer actuators. *Soft Robot.* **7**, 451–461 (2020).
27. J.-H. Youn, H. Mun, K.-U. Kyung, A wearable soft tactile actuator with high output force for fingertip interaction. *IEEE Access* **9**, 30206–30215 (2021).
28. H. Phung, P. T. Hoang, C. T. Nguyen, T. D. Nguyen, H. Jung, U. Kim, H. R. Choi, "Interactive haptic display based on soft actuator and soft sensor," in *Proceedings of the 2017 IEEE/RSJ International Conference on Intelligent Robots and Systems* (IEEE, 2017), pp. 886–891.
29. J.-H. Youn, I. B. Yasir, K.-U. Kyung, "Self-sensing soft tactile actuator for fingertip interface," in *Proceedings of the 2020 IEEE/RSJ International Conference on Intelligent Robots and Systems* (IEEE, 2020), pp. 8939–8944.
30. R. Pelrine, R. Kornbluh, Q. Pei, J. Joseph, High-speed electrically actuated elastomers with strain greater than 100%. *Science.* **287**, 836–839 (2000).
31. E. Hajiesmaili, D. R. Clarke, Dielectric elastomer actuators. *J. Appl. Phys.* **129**, 151102 (2021).
32. Y. Qiu, E. Zhang, R. Plamthottam, Q. Pei, Dielectric elastomer artificial muscle: Materials innovations and device explorations. *Acc. Chem. Res.* **52**, 316–325 (2019).
33. S. Biswas, Y. Visell, Haptic perception, mechanics, and material technologies for virtual reality. *Adv. Funct. Mater.* **31**, 2008186 (2021).
34. V. E. Abraira, D. D. Ginty, The sensory neurons of touch. *Neuron* **79**, 618–639 (2013).
35. G. Corniani, H. P. Saal, Tactile innervation densities across the whole body. *J. Neurophysiol.* **124**, 1229–1240 (2020).
36. M. Morioka, D. J. Whitehouse, M. J. Griffin, Vibrotactile thresholds at the finger, volar forearm, large toe, and heel. *Somatosens. Mot. Res.* **25**, 101–112 (2008).
37. C. Hatzfeld, S. Cao, M. Kupnik, R. Werthschützky, Vibrotactile force perception—Absolute and differential thresholds and external influences. *IEEE Trans. Haptics* **9**, 586–597 (2016).
38. J. Lindsay, R. J. Adams, B. Hannaford, "Improving tactile feedback with an impedance adapter," in *Proceedings of the 2013 World Haptics Conference* (IEEE, 2013), pp. 713–718.
39. Z. Ren, S. Kim, X. Ji, W. Zhu, F. Niroui, J. Kong, Y. Chen, A high-lift micro-aerial-robot powered by low-voltage and long-endurance dielectric elastomer actuators. *Adv. Mater.* **34**, e2106757 (2022).
40. P. A. York, R. J. Wood, "A geometrically-amplified in-plane piezoelectric actuator for mesoscale robotic systems," in *Proceedings of the 2017 IEEE International Conference on Robotics and Automation* (IEEE, 2017), pp. 1263–1268.
41. N. Kellaris, V. Gopaluni Venkata, G. M. Smith, S. K. Mitchell, C. Keplinger, Peano-HASEL actuators: Muscle-mimetic, electrohydraulic transducers that linearly contract on activation. *Sci. Robot.* **3**, eaar3276 (2018).
42. J.-H. Youn, J. S. Koh, K.-U. Kyung, Soft polymer-actuated compliant microgripper with adaptive vibration-controlled grasp and release. *Soft Robot* **11**, 585–595 (2024).
43. M. Wissler, E. Mazza, Mechanical behavior of an acrylic elastomer used in dielectric elastomer actuators. *Sens. Actuator A Phys.* **134**, 494–504 (2007).
44. B. Li, H. Chen, J. Qiang, S. Hu, Z. Zhu, Y. Wang, Effect of mechanical pre-stretch on the stabilization of dielectric elastomer actuation. *J. Phys. D Appl. Phys.* **44**, 155301 (2011).
45. M. W. M. Tan, G. Thangavel, P. S. Lee, Enhancing dynamic actuation performance of dielectric elastomer actuators by tuning viscoelastic effects with polar crosslinking. *NPG Asia Mater.* **11**, 62 (2019).
46. T. Vu-Cong, C. Jean-Mistral, A. Sylvestre, Impact of the nature of the compliant electrodes on the dielectric constant of acrylic and silicone electroactive polymers. *Smart Mater. Struct.* **21**, 105036 (2012).
47. C. Hatzfeld, T. A. Kern, *Engineering Haptic Devices: A Beginner's Guide* (Springer-Verlag, Ed. 2, 2014).
48. C. A. Perez, C. A. Holzmann, H. E. Jaeschke, Two-point vibrotactile discrimination related to parameters of pulse burst stimulus. *Med. Biol. Eng. Comput.* **38**, 74–79 (2000).
49. X. Ji, A. El Haitami, F. Sorba, S. Rosset, G. T. M. Nguyen, C. Plesse, F. Vidal, H. R. Shea, S. Cantin, Stretchable composite monolayer electrodes for low voltage dielectric elastomer actuators. *Sens. Actuator B Chem.* **261**, 135–143 (2018).
50. A. Poulin, S. Rosset, H. R. Shea, Printing low-voltage dielectric elastomer actuators. *Appl. Phys. Lett.* **107**, 244104 (2015).
51. Y. Shi, E. Askounis, R. Plamthottam, T. Libby, Z. Peng, K. Youssef, J. Pu, R. Pelrine, Q. Pei, A processable, high-performance dielectric elastomer and multilayering process. *Science* **377**, 228–232 (2022).

52. C. Cao, R. S. Diteesawat, J. Rossiter, A. T. Conn, "A reconfigurable crawling robot driven by electroactive artificial muscle," in *Proceedings of the 2019 2nd IEEE International Conference on Soft Robotics* (IEEE, 2019), pp. 840–845.
53. X. Ji, X. Liu, V. Cacucciolo, M. Imboden, Y. Civet, A. El Haitami, S. Cantin, Y. Perriard, H. Shea, An autonomous untethered fast soft robotic insect driven by low-voltage dielectric elastomer actuators. *Sci. Robot.* **4**, eaaz6451 (2019).
54. C. Cao, X. Gao, A. T. Conn, Towards efficient elastic actuation in bio-inspired robotics using dielectric elastomer artificial muscles. *Smart Mater. Struct.* **28**, 095015 (2019).
55. Y. Chen, S. Xu, Z. Ren, P. Chirarattananon, Collision resilient insect-scale soft-actuated aerial robots with high agility. *IEEE Trans. Robot.* **37**, 1752–1764 (2021).

Acknowledgments
Funding: This work was supported by the National Research Council of Science and Technology (NST) grant by the Korea government (MSIT) (CRC23021-000) and the internal grant of Electronics and Telecommunications Research Institute (ETRI) (24YB1700, Development of light driven three-dimensional morphing technology for tangible visuo-haptic interaction). **Author contributions:** Conceptualization: J.-H.Y., Q.P., S.Y., and K.-U.K. Methodology: J.-H.Y. and K.-U.K. Investigation: J.-H.Y., S.-Y.J., I.H., and K.-U.K. Resources: J.-H.Y., S.Y., and K.-U.K. Data curation: J.-H.Y. and K.-U.K. Validation: J.-H.Y., I.H., S.Y., and K.-U.K. Formal analysis: J.-H.Y., I.H., and K.-U.K., Software: J.-H.Y., and K.-U.K. Visualization: J.-H.Y., S.Y., and K.-U.K. Supervision: S.Y. and K.-U.K. Writing—original draft: J.-H.Y. and K.-U.K. Writing—review and editing: J.-H.Y., I.H., Q.P., S.Y., and K.-U.K. Funding acquisition: S.Y. and K.-U.K. Project administration: J.-H.Y., S.Y., and K.-U.K. **Competing interests:** J.-H.Y., S.J., I.H., and S.Y. are inventors of patent application US 18/744800 held by Electronics and Telecommunications Research Institute (ETRI). The authors declare that they have no other competing interests. **Data and materials availability:** All data needed to evaluate the conclusions in the paper are present in the paper and/or the Supplementary Materials.

Submitted 30 September 2024
Accepted 7 February 2025
Published 19 March 2025
10.1126/sciadv.adt4839